Computational fluid dynamic simulations of granular flows: insights on the flow-wall interaction dynamics

Francesco Neglia[1,2,3], Fabio Dioguardi[2], Roberto Sulpizio[1], Raffaella Ocone[3], Damiano Sarocchi[4]

[1] Dipartimento di Scienze della Terra e Geoambientali, Università di Bari, Bari, Italy

[2] British Geological Survey, The Lyell Centre, Edinburgh, United Kingdom

[3] Institute of Geoenergy Engineering, Heriot-Watt University, Edinburgh, United Kingdom

[4] Instituto de Geologia, Facultad de Ingeneria, Universidad Autónoma de San Luis Potosí, San Luis Potosì, México

Abstract

Dry volcanic granular flows are gravity-driven currents composed of solid particles where particle-particle interactions dominate the motion. The interaction with topography is a relevant factor controlling the propagation of such flows. In this paper we investigate the dynamics of channelised volcanic granular flows by comparing large-scale experiments with multiphase computational fluid dynamic simulations using the Two-Fluid Model approach, with an emphasis on the dynamics regulating the flow-wall interactions. We use the software MFIX to carry out sensitivity analysis of the boundary conditions for the solid phase implemented in the numerical code. The sensitivity analysis shows how the choice of the boundary condition and of the relevant parameters controlling the boundary conditions highly affect the dynamics of the whole flow. Finally, a preliminary

comparison of the MFIX boundary conditions with the ones obtained from experiments is presented, showing good agreement between the simulated and predicted flow-front velocities.

Keywords

Granular flows, Numerical simulations, MFIX, Boundary conditions

1. Introduction

Granular flows are mixtures of discrete solid particles dominated by grain contacts where the contribution of any interstitial fluid to the flow dynamics is negligible. Those mixtures belong to the family of multiphase flows, which have been extensively studied in a wide range of industrial (fluidised beds, pneumatic transport, etc.) and geophysical (e.g., dry volcanic granular flows, debris avalanches, etc.) applications. Such mixtures, which can be characterised by a wide range of particle sizes, concentrations and materials (Sulpizio et al., 2010; Syamlal et al., 1993), are greatly dissipative due to frictional and inelastic collisions (Boyle and Massoudi, 1989; Dartevelle, 2004; Jaeger et al., 1996).

Specifically, dry volcanic granular flows are generated in different ways and from various sources, such as the collapse of eruptive columns and volcanic domes (Iverson and Vallance, 2001; Sulpizio et al., 2016, 2010). The former are injection into the atmosphere of gas-particles flows (Branney and Kokelaar, 2002) , while the latter consist of magma extruded from a vent that piles up because of its viscosity (Harnett et al., 2018). These types of flows occur frequently in nature and can be hazardous and enormously destructive (e.g. Branney and Kokelaar 2002, Iverson 1997, Louge et al. 2012, Zanchetta et al. 2004); improving the knowledge of their key features would greatly enhance hazard assessment and planning strategies for minimising the impact of these events on the environment.

In recent years, several authors have employed multiphase computational fluid dynamics (CFD) techniques to investigate a variety of processes characterising volcanic flows such like impinging jets (e.g. Valentine and Sweeney 2018), dense granular flows (e.g. Breard et al. 2019, Lube et al. 2019) and collapsing phenomenon (e.g. Valentine 2020). The physical laws governing the flow-wall dynamics implemented in the used CFD models and their effects on the behaviour of the simulated volcanic flows were not investigated. The crucial importance of the boundary conditions to quantitatively predict the granular flow parameters was amply demonstrated by several experiments on the rapid shearing of glass or polymer spheres where granular mixtures with the same density and at the same shear rate, sliding on channel surfaces with different roughness, recorded different shear stresses, velocities and flow rates (Hanes and Inman, 1985; Jop et al., 2005; Sarno et al., 2018a; Savage and Sayed, 1984). Consequently, to investigate the dynamics influencing the flow-wall interaction, we have simulated dense granular flows employing a multiphase CFD solver to understand the role of the implemented boundary conditions.

The multiphase CFD simulation tool used, MFIX (http://mfix.netl.doe.gov/) (Syamlal et al., 1993), provides a suite of models that allows for the simulation of multiphase flows using different approaches, such like the Discrete Element Method (DEM)(Cundall and Strack, 1979; Garg et al., 2012; Li et al., 2012) and the Two-Fluid Model (TFM)(Campbell, 1990; Lun et al., 1984). In DEM the motion of solid particles is simulated by coupling the particles to the fluid flow field using Newton's laws and taking particle-particle and particle-wall interactions into account. In TFM, the solid phase is treated as a fluid whose motion is governed by the Navier-Stokes Equation, with additional models accounting for the rheology of the solid phase, the momentum coupling between the solid and the fluid phase, and the solid-wall interaction. The DEM approach is simpler than the TFM (which relies on a continuum approach), however, storing information for each single particle is computationally expensive and DEM's application is still limited to the analysis of granular material composed of several hundred thousand particles (Ge et al., 2015) –a number which is very small to represent real systems. The heavy computational demand strongly limits the applicability of the DEM to volcanic granular flows, which involve several million of particles with different sizes (from microns to meters), densities (from hundreds to few thousand of kg m^{-3}) and shapes (from almost spherical to highly irregular) (Neglia et al., 2020). To date the TFM approach remains the more feasible one for these kinds of flows.

In the present work, we first explore the existing relationships implemented in TFM MFIX by focusing on the boundary conditions for the solid phase. We investigate these boundary conditions describing the dynamic interaction between the solid phase and a rigid wall. We then undertake a sensitivity analysis focusing on the parameters appearing in the solid-wall boundary conditions. Finally, we apply MFIX to replicate a large-scale experiment on volcanic dry granular mixture flowing in an inclined channel; by using the knowledge carried out by the sensitivity analysis, we set-up the optimum MFIX simulations configuration.

2. From theory to an optimal MFIX configuration: sensitivity analyses of wall boundary conditions

In this section we introduce 1) the TFM implemented in MFIX and 2) the boundary conditions (BC) controlling the interaction between the solid phase and a wall.

2.1. Two-Fluid Model governing equations

The TFM treats the gas and solid phase as interpenetrating continua, whose motion is solved using the Eulerian-Eulerian approach. Flow variables are volume-averaged over a region (named control volume -CV) that is large when compared to the particle size but small compared to the scale of macroscopic variations inside the flow domain (Anderson and Jackson, 1967). In the TFM, the Navier-Stokes equations for the conservation of mass, momentum and energy for each phase are solved, with constitutive equations accounting for the interphase interactions. In the following we do not report the energy conservation equations since in this study we consider the flow isothermal. The mass conservation equations for gas and mth solid phase are:

$$\frac{\partial(\varepsilon_g \rho_g)}{\partial t} + \nabla \cdot \left(\varepsilon_g \rho_g \boldsymbol{U_g}\right) = 0 \tag{1}$$

$$\frac{\partial(\varepsilon_{sm} \rho_{sm})}{\partial t} + \nabla \cdot (\varepsilon_{sm} \rho_{sm} \boldsymbol{U_{sm}}) = 0 \tag{2}$$

where ρ is the density, ε is the volume concentration, U is the velocity and the subscripts s and g denote the solid and fluid phase, respectively. All symbols are listed in Table 1. The first term on the left-hand side accounts for the rate of mass change per unit volume, and the second one is the convective mass flux. Potential sources and sinks due to phase changes and chemical reactions are neglected.

The momentum equations for the gas and solid phase are:

$$\frac{\partial(\varepsilon_g \rho_g \boldsymbol{U_g})}{\partial t} + \nabla \cdot \left(\varepsilon_g \rho_g \boldsymbol{U_g} \boldsymbol{U_g}\right) = \nabla \cdot \boldsymbol{\tau_g} + \varepsilon_g \rho_g \boldsymbol{g} - \sum_{m=1}^{M} \boldsymbol{I_{gm}} \tag{3}$$

$$\frac{\partial(\varepsilon_{sm} \rho_{sm} \boldsymbol{U_{sm}})}{\partial t} + \nabla \cdot (\varepsilon_{sm} \rho_{sm} \boldsymbol{U_{sm}} \boldsymbol{U_{sm}}) = \nabla \cdot \boldsymbol{\tau_{sm}} + \varepsilon_{sm} \rho_{sm} \boldsymbol{g} + \boldsymbol{I_{gm}} + \sum_{\substack{l=1 \\ l \neq m}}^{M} \boldsymbol{I_{ml}} \tag{4}$$

here $\boldsymbol{\tau_g}$ and $\boldsymbol{\tau_{sm}}$ are the fluid and solid phase stress tensor, respectively, $\boldsymbol{g}$ is the gravitational acceleration, $\boldsymbol{I_{gm}}$ represents the transferred momentum between the gas phase and the mth solids phase and $\boldsymbol{I_{ml}}$ is the interaction force between the mth and lth solid phase. The first and the second term on the left-hand side (Eq. 3 and 4) represent the net rate of momentum change and the net rate of momentum transferred by convection, respectively, and the first and second term on the right-hand side (Eq. 3 and 4) represent the internal stress and the body forces, respectively.

Johnson and Jackson (Johnson and Jackson, 1987) proposed a model to describe the kinetic and frictional stresses that contribute to the solid stress tensor $\boldsymbol{\tau_{sm}}$, where the kinetic contribution is calculated applying the kinetic theory to the granular material (Boyle and Massoudi, 1989) and the frictional contribution is computed by means of the rigid-plastic rheological model proposed by Schaeffer (Schaeffer, 1987). MFIX combines the two theories by considering a "switch" value represented by the void fraction at maximum packing ε_g^* (Syamlal et al., 1993):

$$\boldsymbol{\tau_{sm}} = \begin{cases} -P_{sm}^f \boldsymbol{I} + 2\mu_{sm}^f \boldsymbol{S} & \varepsilon_g \leq \varepsilon_g^* \\ (-P_{sm}^k + \eta\mu_b \nabla \cdot \boldsymbol{v_s})\boldsymbol{I} + 2\mu_{sm}^k \boldsymbol{S} & \varepsilon_g > \varepsilon_g^* \end{cases} \tag{5}$$

where P_{sm}^f and P_{sm}^k are the solid pressure for the frictional and kinetic-collisional regime, respectively, $\boldsymbol{I}$ is the unit tensor, $\boldsymbol{S}$ is the strain rate tensor, $\eta = (1 + e_p)/2$ with e_p being the particle-particle coefficient of restitution, μ_{sm}^k and μ_{sm}^f are the kinetic and solid viscosity, respectively, and μ_b is the bulk viscosity. The higher e_p, the lower the dissipation rate given by inelastic collisions. Similar to e_p, there is a restitution coefficient for particle-wall collision (e_w).

The solid pressure P_{sm}^{k} originates from the particles' kinetic interactions and is modelled as:

$$P_{sm}^{k} = \varepsilon_{sm}\rho_{sm}\theta_{m}\left(1 + 4\eta \sum_{n=1}^{M} \varepsilon_{sn} g_{0,mn}\right) \quad 6$$

where g_0 is the radial distribution function, which quantifies the probability of finding two particles at that specific location (Boyle and Massoudi, 1989) and acts as a correcting factor when the concentration is high enough to break the molecular chaos assumption (Dartevelle, 2004) and θ is the granular temperature, which quantifies the agitation state of the particles. θ is proportional to the mean quadratic fluctuating velocity due to the random motion of the particles:

$$\frac{3}{2}\theta_{m} = \frac{1}{2}\langle \boldsymbol{c}_{\boldsymbol{m}}^{\prime 2} \rangle \quad 7$$

where $\boldsymbol{c}'_{\boldsymbol{m}}$ is the fluctuating component of the instantaneous velocity $\boldsymbol{C}_{\boldsymbol{m}}$ of the mth solid phase defined as $\boldsymbol{C}_{\boldsymbol{m}} = \boldsymbol{U}_{\boldsymbol{sm}} + \boldsymbol{c}'_{\boldsymbol{m}}$. The term on the right-hand side of Eq. 7 defines the granular energy of the continuum.

The solid pressure P_{s}^{f} is calculated using the model proposed by Schaeffer (1987) for a plastic flow of a granular medium occurring at critical state, i.e. when the solid volume concentration exceeds the maximum packing. The Schaeffer model is based on plastic flow theory of Jenike (1987), who used an arbitrary function to take into account a certain amount of compressibility in the solid phase (Pritchett et al., 1978) and to prevent unphysically large solids volume concentration (Gera et al., 2004). The Schaeffer model was implemented in MFIX by Syamlal et al. (1993) as:

$$P_s^f = P^* = A\left(\varepsilon_g^* - \varepsilon_g\right)^{10} \tag{8}$$

where A is a constant taken equals to 10^{24} Pa and P^* represents the solid pressure at the critical state.

More recently, the Princeton model (Srivastava and Sundaresan, 2003) for solid pressure calculation, was implemented in MFIX. The Princeton model starts from the quasi-static model proposed by Schaeffer and modifies it to account for strain rate fluctuations associated with the generation of shear layers that decrease the shear stress in the granular material (Savage, 1998). In this way, numerical singularities are avoided in the region where $\boldsymbol{S} = 0$ as long as $\theta \neq 0$. The solid pressure P_s^f can be expressed as:

$$P_s^f = P^* \left(1 - \frac{\nabla \cdot \boldsymbol{U}_s}{N\sqrt{2}\sin\delta_{int}\sqrt{\left(\boldsymbol{S}:\boldsymbol{S} + \frac{\theta}{d^2}\right)}}\right)^{\frac{1}{N-1}} \tag{9}$$

$$P^* = \begin{cases} A\left(\varepsilon_g^* - \varepsilon_g\right)^{10} & \varepsilon_g < \varepsilon_g^* \\ Fr\,\frac{\left(\varepsilon_s - \varepsilon_s^{min}\right)^B}{\left(\varepsilon_s^* - \varepsilon_s\right)^C} & \varepsilon_g^* \leq \varepsilon_g < \left(1 - \varepsilon_s^{min}\right) \\ 0 & \varepsilon_g \geq \left(1 - \varepsilon_s^{min}\right) \end{cases} \tag{10}$$

where ε_s^{min} is equal to 0.5, δ_{int} is the internal friction angle, d is the particles diameter, Fr and the exponents B and C are constants equal to 0.05 Pa, 2 and 5, respectively. The exponent N is equal to $\sqrt{3}/2\, sin\, sin\, \delta_{int}$ in dilatation conditions ($\nabla \cdot \boldsymbol{U_s} \geq 0$) or equal to 0 in compaction conditions ($\nabla \cdot \boldsymbol{U_s} < 0$). The strain rate fluctuations are represented by the term θ/d^2. If the granular material is compacted, the solid pressure will be equal to the critical pressure P^*. For all the simulations discussed in the present paper, the Princeton frictional model was selected because tests on the two frictional models conducted by Breard et al. (2019), showed that the Princeton model leads to a more gradual variation of P_s^f and to a better dissipation of the pore pressures compared to what obtained with the Schaeffer one.

The particles agitation state can be quantified by means of the granular temperature θ (Eq. 7). The conservation equation of the granular energy (right-hand side term of Eq. 7) is given by:

$$\frac{3}{2}\rho_{sm}\left(\frac{\partial(\varepsilon_{sm}\theta_m)}{\partial t} + \nabla\cdot(\varepsilon_{sm}\theta_m\boldsymbol{U_{sm}})\right) = -\nabla\cdot\boldsymbol{q_m} + \boldsymbol{\tau_{sm}}:\nabla\cdot\mathbf{U_{sm}} - \gamma_{\theta_m} + \varphi_{gm} + \sum_{\substack{l=1\\ l\neq m}}^{M}\varphi_{lm} \qquad 11$$

where $\boldsymbol{q}$ is the diffusive flux of granular energy, γ_θ is the granular energy dissipation due to inelastic collisions, φ_{gm} represents the transferred granular energy between gas and the mth solids phase and φ_{lm} accounts for the transferred granular energy between the mth and lth solid phases. The terms on the left-hand side are the rate of change and the advection of the granular temperature, respectively. The first term on the right-hand side (Eq. 11) is the diffusive transport of granular energy, the second term is the net rate of granular energy produced by shear and the last three terms represent dissipation of granular energy.

Symbol	Description	Dimension

A	constant of Eq. 10	Pa
B	constant of Eq. 10	-
c_w	source term in Eq. 14 due to particle-wall slip	kg s^{-3}
C	constant of Eq. 10	-
$\boldsymbol{C_m}$	instantaneous velocity	m s^{-1}
$\boldsymbol{c'_m}$	fluctuating component of $\boldsymbol{C_m}$	m s^{-1}
d	particle diameter	m
D	dissipation rate of granular energy due to inelastic collisions	kg s^{-3}
e_p	restitution coefficient for the particle-particle collision	-
e_w	restitution coefficient for the particle-wall collision	-
Fr	constant of Eq. 12	Pa
$\boldsymbol{g}$	gravitational acceleration	m s^{-2}
h_w^u	wall velocity transfer coefficient	m^{-1}
h_w^θ	wall granular temperature transfer coefficient	kg m^{-2} s^{-1}
$\boldsymbol{I}$	unit tensor	-
$\boldsymbol{I_{gm}}$	momentum transfer from fluid phase to mth solid phase	kg m^{-2} s^{-1}
$\boldsymbol{I_{ml}}$	momentum transfer from mth to lth solid phase	kg m^{-2} s^{-1}
k	function of wall friction angle and restitution coefficient	-
$\overline{M_{t,w}}$	average tangential momentum transferred per collision	kg m s^{-1}

n	fluid-to-wall normal	-
n_1	wall-to-fluid normal	-
N	function of internal friction angle	-
P	pressure	Pa
$\boldsymbol{q}$	diffusive flux of granular energy	kg s^{-3}
r	normalized slip velocity at the wall	-
$\boldsymbol{S}$	strain rate tensor	s^{-1}
t	time	s
$\boldsymbol{U}$	velocity	m s^{-1}
U_{mg}	solid velocity magnitude	m s^{-1}
$\boldsymbol{U_{sl}}$	slip velocity	m s^{-1}

Greek symbol	Description	Dimension
γ_θ	granular energy dissipation due to inelastic collisions	kg s^{-3}
δ_{int}	internal friction angle of the granular material	° (degree)
δ_w	Wall friction angle of the granular material	° (degree)
ε	volume concentration	-
η	function of the inelastic collision	-
θ	granular temperature	m^2 s^{-2}
μ	viscosity	Pa s

μ_b	bulk viscosity	Pa s
ρ	density	kg m^{-3}
φ_{gm}	transferred granular energy between gas and mth solid phase	kg s^{-3}
φ_{lm}	transferred granular energy between mth and lth solid phase	kg s^{-3}
ϕ	specularity coefficient	-
ϕ_0	specularity coefficient when r goes to zero	-
Subscripts		
g	fluid phase	
m	solid phase mth	
s	solid phase	
w	wall	
Superscript		
f	frictional	
min	minimum concentration referred to the Princeton model	
k	kinetic	
$*$	maximum packing	

Table 1. List of symbols with description and physical dimension.

2.2 Boundary conditions available in MFIX

The following boundary conditions for the conservation equations of the gas and solid phases are considered in MFIX: no-slip (zero velocity at the wall), free-slip (velocity gradient vanishes at the wall) and partial-slip wall condition, which controls the trend of velocity for the gas and solid phases and of the granular temperature from the flow to the wall:

$$\frac{dU}{dn} + h_w^u(U - U_w) = 0 \tag{12}$$

$$\frac{d\theta}{dn} + h_w^\theta(\theta - \theta_w) = c_w \tag{13}$$

where c_w is the source term due to particle-wall slip, U_w and θ_w are the velocity and granular temperature at the wall, n is the fluid-to-wall normal, and h_w^θ and h_w^u are the transfer coefficients, which regulate the spatial rate with which U and θ approximate U_w and θ_w.

The parameters in the partial-slip boundary conditions can be defined in in two different ways: user-defined values that apply to all the walls in the whole computational domain or local flow-dependent values calculated for the solid phase by means of the Johnson and Jackson (1987) or Jenkins (1992) models.

Johnson and Jackson (1987) developed a condition for the slip velocity of particles relative to a wall by equating the tangential force per unit area exerted on the wall by the particles to the stress due to the granular assembly close to the boundary:

$$\frac{\boldsymbol{U_{sl}}\boldsymbol{\tau_{sm}}\boldsymbol{n_1}}{|\boldsymbol{U_{sl}}|} + \frac{\phi\sqrt{3\theta}\pi\rho_s\varepsilon_s|\boldsymbol{U_{sl}}|}{6\varepsilon_s^*\left[1-\left(\frac{\varepsilon_s}{\varepsilon_s^*}\right)^{\frac{1}{3}}\right]}, + P_s^f\tan\delta_w = 0 \tag{14}$$

where $\boldsymbol{n_1}$ is the boundary-to-flow unit normal vector, U_{sl} is the slip velocity relative to the wall and ϕ is the specularity coefficient, which varies between zero for perfectly specular collision and unity for perfectly diffuse collisions (Johnson and Jackson, 1987) and depends on the particle and wall properties (including the surface roughness) (Li et al., 2010b). Specular and diffuse collisions correspond to smooth and rough walls, respectively (Hui et al., 1984). The first term of Eq. 14 represents the stress in the granular flow approaching the boundary, the second term is the rate of tangential momentum transferred to the wall by particles collisions and the third term represents the frictional stress due to the sliding particles, which is calculated by applying Coulomb friction law to the particles that slide at the boundary (Li and Benyahia, 2012).

The specularity coefficient ϕ can be also explained as the fraction of the collision that transfer significant amount of average tangential momentum to the wall (Hui et al., 1984):

$$\overline{M_{t,w}} = \phi\rho_s\pi d^3\, U_{sl}/6 \qquad 15$$

Li and Benyahia (Li and Benyahia, 2012) proposed a predictive expression for ϕ, which was obtained from numerical integration data based on the rigid-body theory:

$$\phi = \begin{cases} -7\sqrt{6\pi}(\phi_0)^2 r + \phi_0 & r \le \frac{4k}{7\sqrt{6\pi}\phi_0} \\ \frac{2}{7}\frac{k}{r\sqrt{6\pi}} & r > \frac{4k}{7\sqrt{6\pi}\phi_0} \end{cases} \qquad 16$$

where r is equal to $U_{sl}/\sqrt{3\theta}$ (the normalized slip velocity at the wall characterizing the mean impact angle of particles), k is equal to $\frac{7}{2}\tan\delta_w\,(1+e_w)$ and ϕ_0 states for ϕ value when r goes to zero:

$$\phi_0 = -0.0012596 + 0.1064551k - 0.04281476k^2 + 0.0097594k^3 - 0.0012508258k^4 + 0.0000836983k^5 - 0.00000226955k^6 \tag{17}$$

The Johnson and Jackson boundary condition with Li and Benyahia modification for the calculation of ϕ is referred to in this paper as "revisited Johnson and Jackson BC".

The boundary condition for the granular energy is obtained from the balance of granular energy over a control volume (Johnson and Jackson, 1987):

$$-\boldsymbol{n_1} \cdot \boldsymbol{q} = D + \boldsymbol{U_{sl}} \cdot \boldsymbol{S_c^b} \tag{18}$$

where $\boldsymbol{S_c^b}$ corresponds to the second term of Eq. 14 and D is the rate of dissipation of granular energy due to inelastic particles-wall collisions, which is given by:

$$D = \frac{1}{4}\pi\rho_s\theta(1 - e_w^2)\frac{\sqrt{3\theta}}{\left[\left(\frac{\varepsilon_s^*}{\varepsilon_s}\right)^{\frac{1}{3}} - 1\right]}\frac{1}{\left(\frac{\varepsilon_s^*}{\varepsilon_s}\right)^{\frac{2}{3}}} \tag{19}$$

The model proposed by Jenkins (1992) consists of relationships for the shear stress and granular energy flux at the wall in two limiting case: small-friction/all-sliding limit and the large-friction/no-sliding limit. The only limit case currently implemented in MFIX is the small-friction/all-sliding limit, for which all collisions involve sliding and the ratio of shear to normal stress, is equal to the wall friction coefficient:

$$\frac{q}{P_s^k\sqrt{3\theta}} = \tan^2\delta_w\,(1+e_w)\frac{21}{16} - \frac{3}{8}(1-e_w) \qquad 20$$

To better understand the effect of h_w^u, h_w^θ and c_w on the solid-wall interactions in the simulations, we analytically solved Eqs. 12 and 13 and plotted the U and θ vs. n (Fig. 1), setting for the velocity profile equation (Eq. 12) U = 5.0 m s^{-1} and U_w = 0.0 m s^{-1} and for granular temperature profiles equation (Eq. 13) θ = 0.5 m^2 s^{-2} and θ_w = 0.01 m^2 s^{-2}.

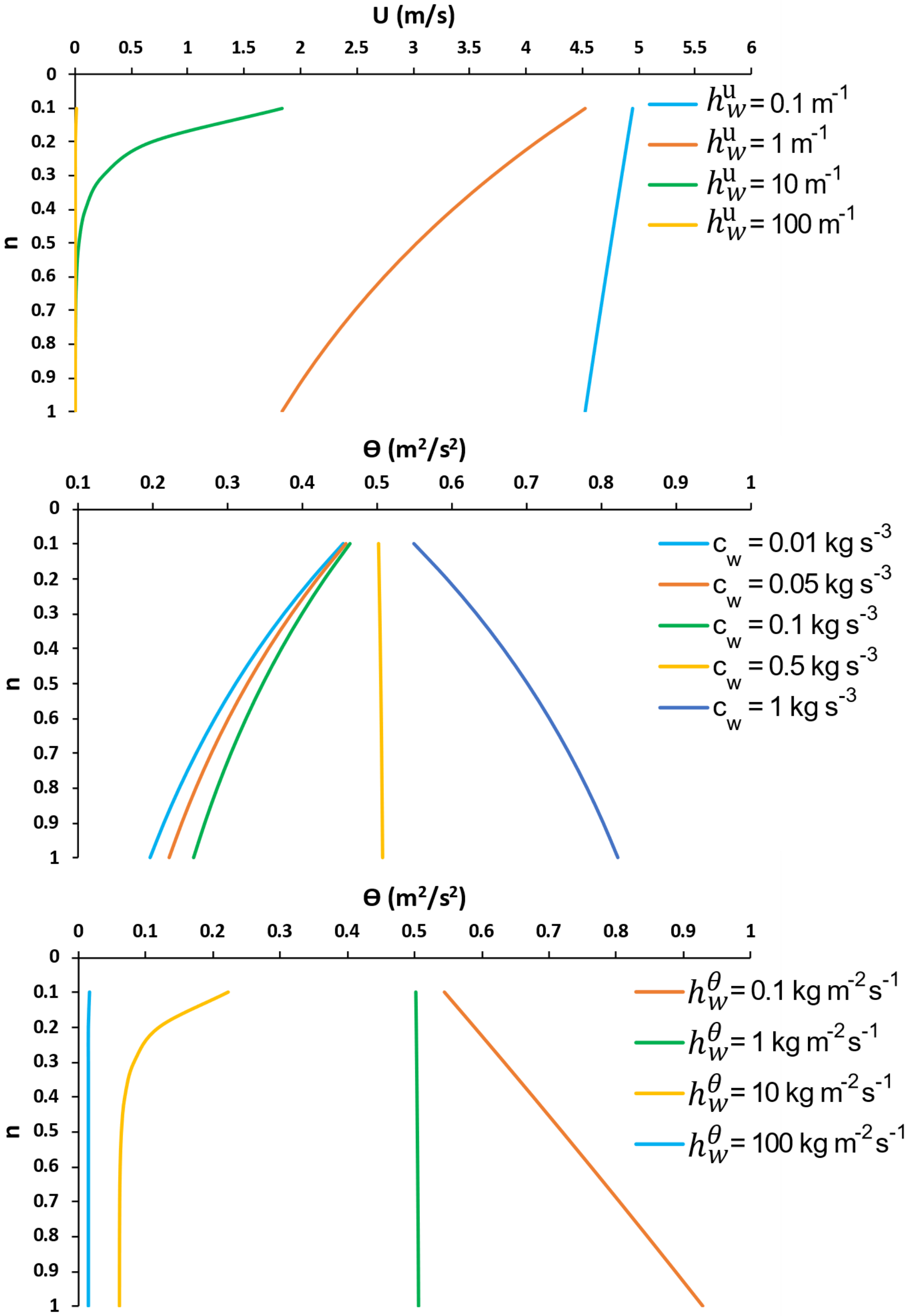

Figure 1. Flow velocities (U) and granular temperatures (θ) plotted against the normal fluid-to-wall (n).

Figure 1 shows that the higher h_w^u, the sharper the velocity gradients. Indeed, h_w^u = 0.1 m^{-1} yields a velocity gradient with constant angular coefficient resulting in high velocities (close to U = 5 m s^{-1}), whereas h_w^u = 100 m^{-1} results in velocities equal to U_w (0.0 m s^{-1}), freezing the particle at the wall. Therefore, in the limit of h_w^u approaching 0 the partial-slip boundary condition reduces to a free-slip condition for the solid phase; on the other hand, large values of h_w^u leads to a no-slip condition. Furthermore, h_w^u ranging between 1 – 10 m^{-1} produces concave velocity profiles facing to the right.

h_w^θ and c_w show two different trends at changing θ. For $h_w^\theta > 1$ kg m^{-2}s^{-1} and $c_w < 0.5$ kg s^{-3} the granular temperatures decrease more or less quickly in the direction towards the wall, whereas for $h_w^\theta < 1$ kg m^{-2}s^{-1} and $c_w > 0.5$ kg s^{-3} an opposite trend is observed and the granular temperature increases at the wall. The inverse trend is physically unrealistic when compared to granular flows where the basal part is dominated by enduring contacts between particles (Sulpizio et al., 2016). Indeed, $h_w^\theta = 10$ kg m^{-2}s^{-1} and $c_w \leq 0.1$ kg s^{-3} result in profiles closer to the experimentally measured ones (Sarno et al., 2018b).

Partial-slip wall condition	Johnson and Jackson (1987)	Jenkins (1992)
$\frac{dU}{dn} + h_w^u(U - U_w) = 0$ *where* $h_w^u = \frac{COL}{\mu_s^k}$ $\quad \varepsilon_s \leq \varepsilon_s^{min}$ $h_w^u = \frac{COL+FRI}{\mu_s^k+\mu_s^f}$ $\quad \varepsilon_s > \varepsilon_s^{min}$	$COL = \frac{\boldsymbol{\phi}\sqrt{3\theta}\pi\rho_s\varepsilon_s g_0}{6(1-\varepsilon_s^*)}$	$COL = \frac{\tan\delta_w \; P_s^k}{\boldsymbol{U_{sl}}}$
$\frac{d\theta}{dn} + h_w^\theta(\theta - \theta_w) = c_w$	$h_w^\theta = \frac{1}{4}\pi\rho_s(1-e_w^2)\frac{\sqrt{3\theta}}{(1-\varepsilon_s^*)}$ $c_w = \boldsymbol{U_{sl}} \cdot \boldsymbol{S_c^b}$	$h_w^\theta = \frac{3}{8}(1-e_w)P_s^k\sqrt{3\,\theta}\frac{1}{\theta}$ $c_w = \tan^2\delta_w(1+e_w)\frac{21}{16}P_s^k\sqrt{3\,\theta}$

Table 2. Summary of the partial-slip wall conditions as implemented in MFIX. COL and FRI represent collisional and frictional contribute to the wall, respectively. FRI is equal for the Johnson and Jackson and Jenkins boundary conditions, i.e. equals to the Coulomb law.

2.2.1 Sensitivity analysis of the boundary conditions for the solid phase

In sections 2.2.2, 2.2.3 and 2.2.4, we present results of the sensitivity analysis of the wall boundary conditions for the solid phase. We first focus on the effect of varying the specularity coefficient when using the Johnson and Jackson BC (Johnson and Jackson, 1987). We then analyse the influence of particle size on the simulated flows using Jenkins (Jenkins, 1992). We also show the effect of manually changing the parameters of the partial-slip boundary condition h_w^{θ}, h_w^{u} and c_w (Eqs. 12 and 13). Finally, we compare results obtained by the different configurations of the partial-slip wall condition in MFIX (manual, Johnson and Jackson, Jenkins). In all the simulations discussed in Section 2.2.2, 2.2.3 and 2.2.4, the computational domain consists of a rectangle of 20.0 m length x 1.8 m height discretized with a finer grid with rectangular cells of 0.02 m x 0.005 m in the focus area and by a coarser one close to the walls (Fig. 2).

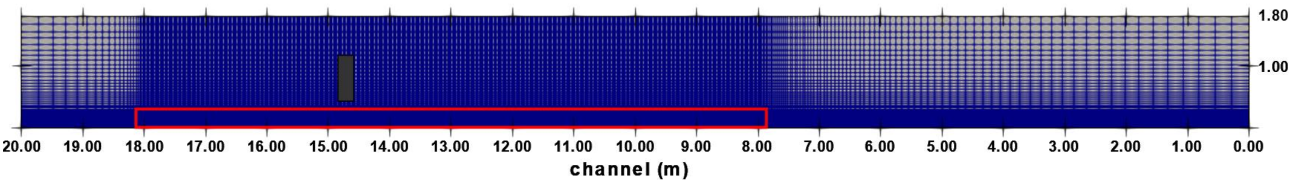

Figure 2. Grid layout for the computational domain. The granular material is shaded grey and the focus area is outlined by the solid red line.

The simulations were carried out by dropping granular material from a height of 0.40 m on a 40° sloped channel. This was reproduced through tilting the components of gravity acceleration at the instant of granular material impacting on the channel surface (Fig. 3). The physical parameters for the solid and fluid phases are reported in Table 3.

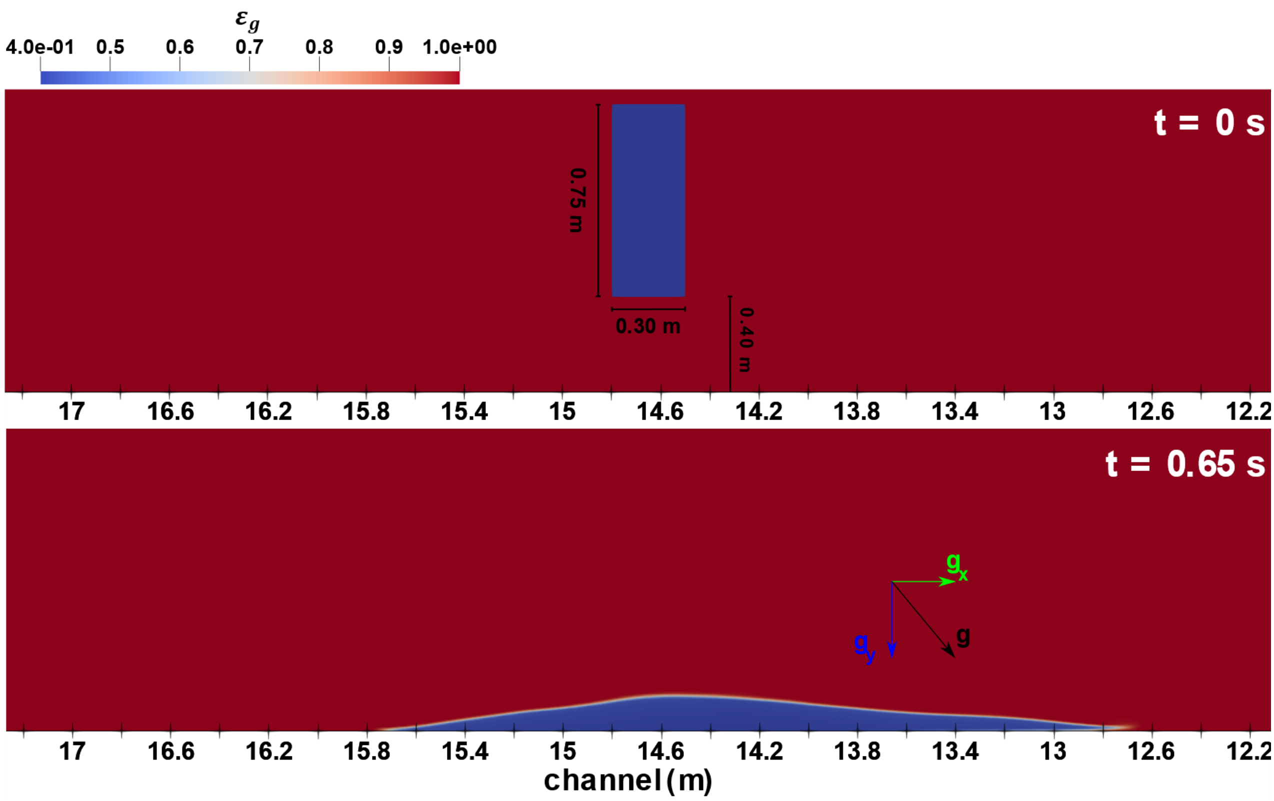

Figure 3. Gas volume concentration (ε_g) at t=0 s and t=0.65 s. The green and blue arrows denote the gravitational accelerations in the x and y direction, while the black arrow indicates the resulting gravitational acceleration.

Parameters (unit)	Sensitivity analysis	Experimental granular flow simulations

Solid density (kg/m^3)	2000	2300
Particles diameter (m)	0.1-0.5-1 x 10^{-3}	1 x 10^{-3}
Particle-particle restitution coefficient	0.9	0.9
Particle-wall restitution coefficient	0.7	0.7
Internal friction angle (°)	35°	33°
Basal friction angle (°)	11°	11°
Max packing fraction	0.65	0.65
Fluid density (kg/m^3)	1.2	1.2
Fluid dynamic viscosity (Pa s)	1.8 x 10^{-5}	1.8 x 10^{-5}

Table 3. Solid and fluid phase parameters used in the simulations.

2.2.2 Sensitivity analysis of Johnson and Jackson boundary condition to specularity coefficient and particles diameter

Simulations of a mono-disperse granular flow sliding on a 40° sloped channel were carried out varying the value of the specularity coefficient ϕ and the particle diameter d. For the simulations at varying ϕ the solid phase size was set to 0.5 mm, while for the simulations at changing d the specularity coefficient was set to 0.1. Profiles of solid volume concentration, solid velocity in x-direction (u_s) and granular temperature at a simulation time (t) of 1.25 s are reported in Figure 4.

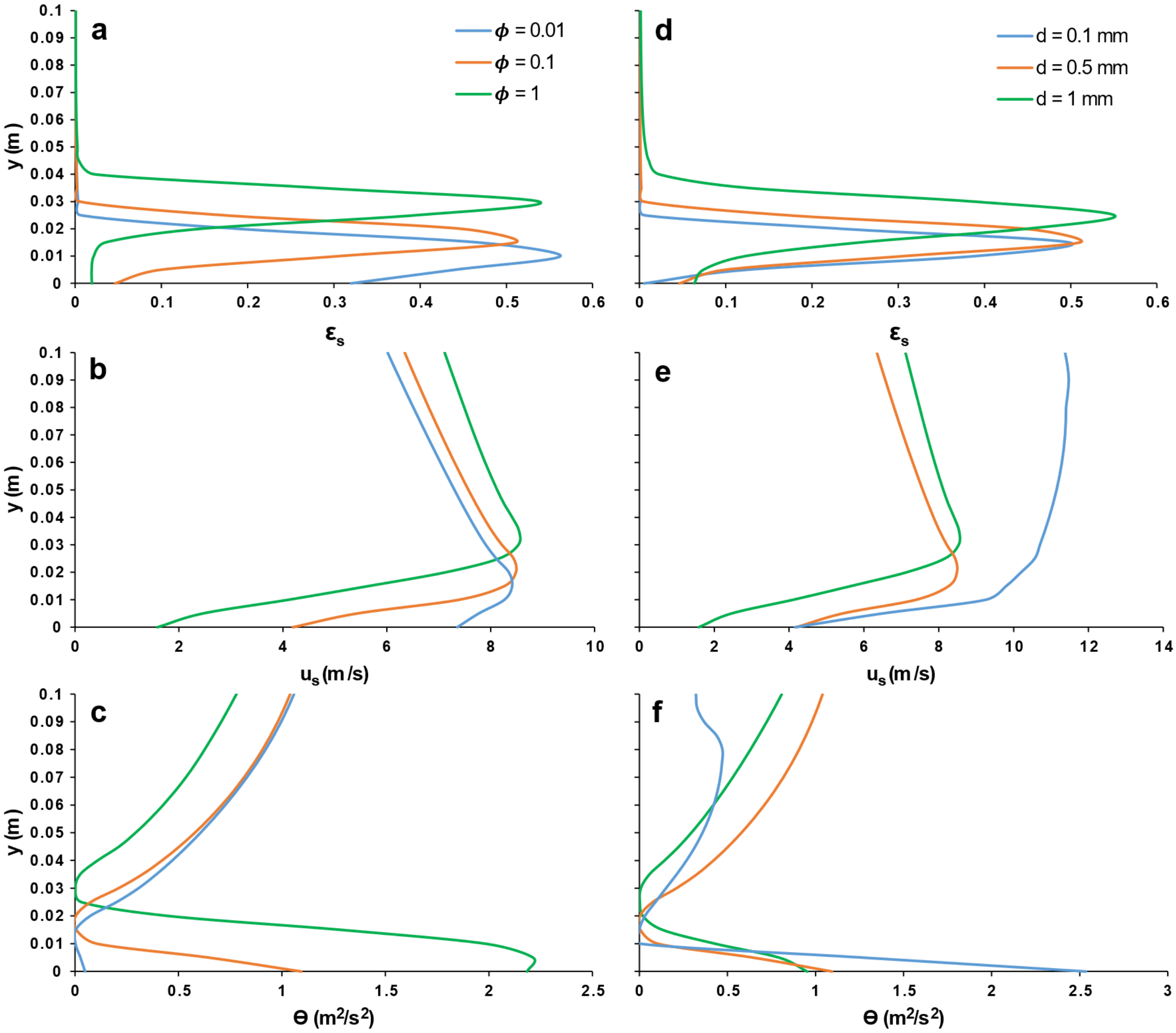

Figure 4. Profiles of solid volume concentration (a, d), solid velocity in x-direction (b, e) and granular temperature (c, f) at 9 m from the right side of the domain (or 5.5 m downstream the initial position of the granular material) against the distance from the wall at changing ϕ and d.

The vertical profiles of ε_s (Figs. 4a and 4d) show the formation of a flow basal layer at the wall where particle concentration is less than the peak concentration in the flow. Hereafter we refer to this feature as "air-cushion". We observed that the air-cushion is sensitive to the particles diameters and to the specularity coefficient. In fact, the greater ϕ and d, the thicker the air-cushion at the flow base. In particular, ϕ has a greater impact on the air-cushion, with values of ε_s at the wall that range from 0.03 (ϕ = 1) to 0.32 (ϕ = 0.01) and thickness ranging between 0.01 m – 0.03 m (Fig. 4a).

Velocity profiles of the solid phase in the x-direction (u_s) exhibit maximum velocities that range from 8.4 m s^{-1} to 8.5 m s^{-1} (Figs. 4b and 4e), with the exception of the maximum velocity of 11.45 m s^{-1} recorded by the granular flow with particles diameter of 0.1 mm (Fig. 4e). For all the simulations, u_s linearly decreases from the maximum to the top of the flow (Fig. 4b). The air-cushion affects u_s at the wall increasing its gradient.

θ is significantly influenced by changing ϕ and d, with the highest values of 2.2 m^2 s^{-2} and 2.5 m^2 s^{-2} at the wall obtained for ϕ = 1 and d = 1 mm, respectively (Figs. 4c and 4f). All profiles show a minimum of the granular temperature in the region where ε_s and u_s are at their peak (Figs. 4b and 4e), while θ increases towards the top of the flow where ε_s decreases. This can be attributed to the particle fluctuations being inhibited or almost suppressed in the most concentrated regions of the flow where ε_s is maximum, and enhanced in the top and basal part of the flow that is more diluted.

2.2.3 Particle diameter sensitivity analysis of Jenkins boundary condition

The specularity coefficient is not used in the Jenkins boundary condition (see Table 2 and Eq. 20) and, hence, we focused on the effects of varying the solid particles mean size. Profiles of gas and solid volume concentration, solid velocity in the x-direction and granular temperature at t of 1.25 s are reported in Figures 5.

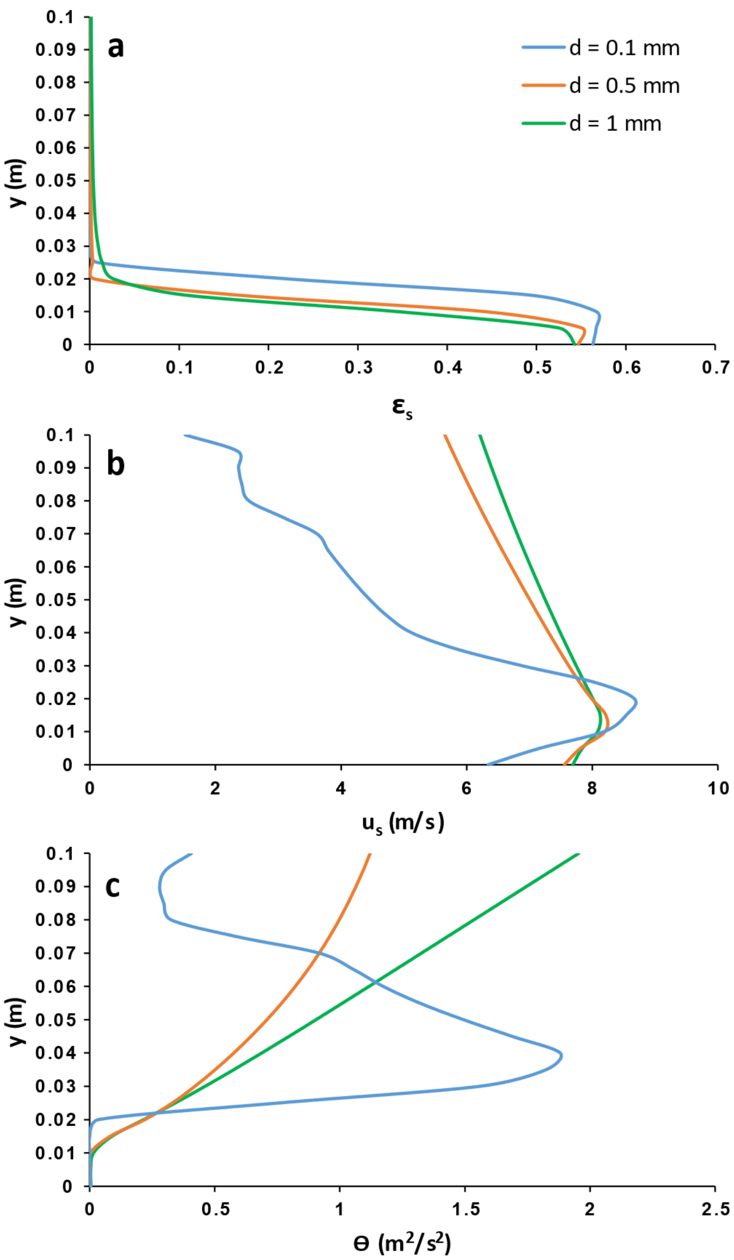

Figure 5. Profiles of solid volume concentration (a), solid velocity in x-direction (b) and granular temperature (c) at 9 m from the right side of the domain (or 5.5 m downstream the initial position of the granular material) against the distance from the wall at changing d.

ε_s profiles and plots show flow thickness ranging between 0.020 m – 0.026 m with the thickest simulated flow obtained with the smallest particles (d = 0.1 mm) (Figs. 5a). In particular, the profiles do not exhibit the air-cushion at the flow base, which can then be attributed to the Johnson and Jackson boundary condition. The vertical u_s profiles exhibit maximum velocities ranging between

8.18 m s^{-1} – 8.67 m s^{-1}, with the highest velocity for d = 0.1 mm (Fig. 5b). All θ profiles are characterised by a basal region with θ = 0 m^2 s^{-2}, which coincides with the concentrated part of the simulated flow (Fig. 5c). θ profile for d = 0.1 mm exhibits the most relevant variations with regards to profiles for d = 0.5 mm – 1 mm, recording a peak at around 40% of the flow thickness in proximity of the diluted part of the flow, which enhances the particle fluctuations.

2.2.4 Sensitivity analysis to user-defined h_w^θ, h_w^u, c_w

The Johnson and Jackson (1987) and Jenkins (1992) boundary conditions for solid phase (Table 2) are used in MFIX to calculate the local flow-dependent values of h_w^θ, h_w^u and c_w coefficients, which are required by the partial-slip wall condition equations (Eqs. 12 and 13). To better understand the role played by these coefficients in controlling the simulated granular flows and the solid phase-wall dynamics, we carried out simulations of mono-disperse granular flows with particle size of 0.5 mm by manually setting h_w^θ, h_w^u and c_w to all the wall in the whole computational domain and for the entire duration of the simulation. Plots of gas volume concentration and vertical profiles of solid volume concentration, solid velocity in the x-direction and granular temperature at t of 1.25 s are reported in Figures 6 and 7.

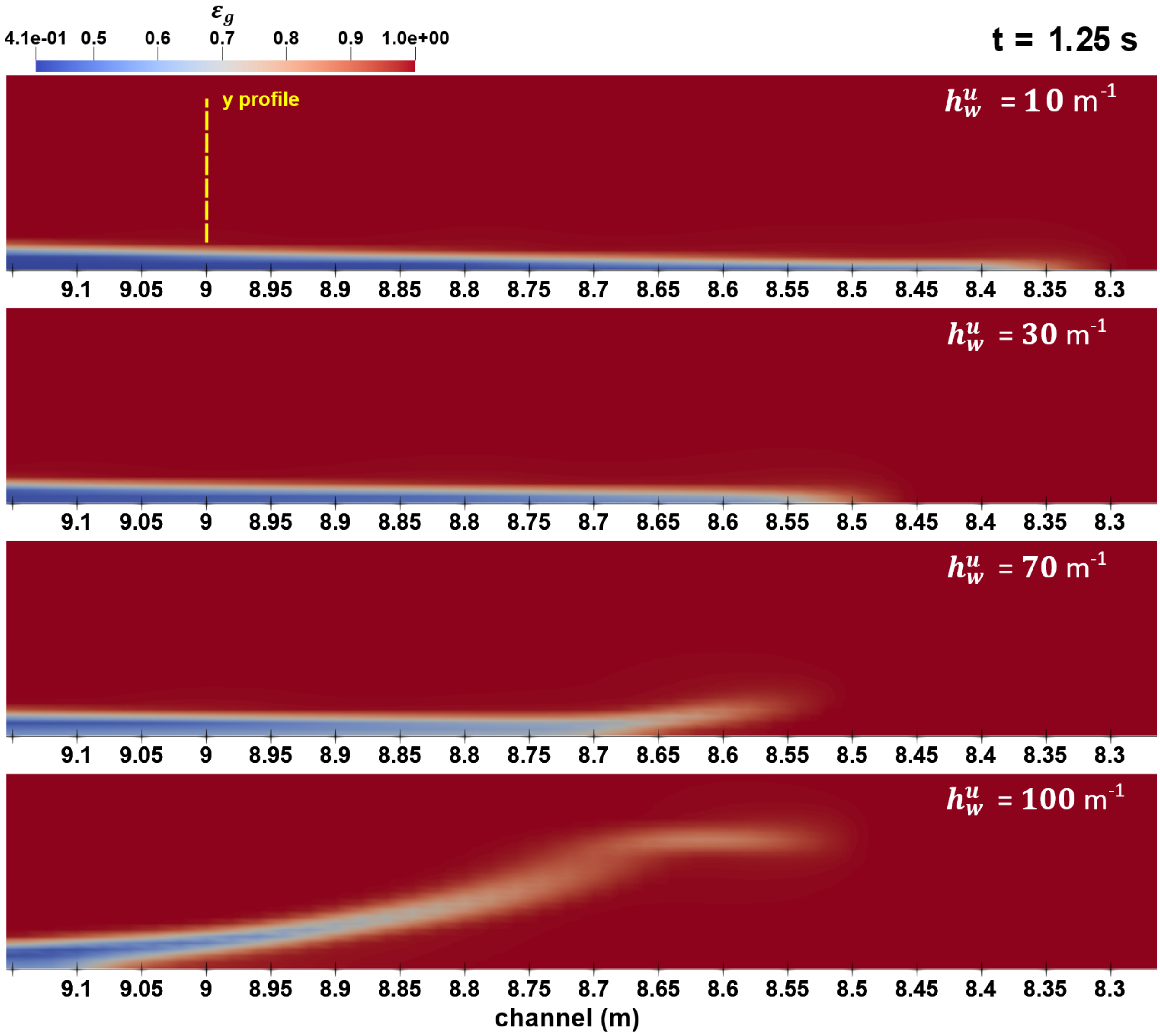

Figure 6. Plots of gas volume concentration (ε_g) at changing h_w^u. The yellow dotted line marks the profiles position shown below. t = simulation time.

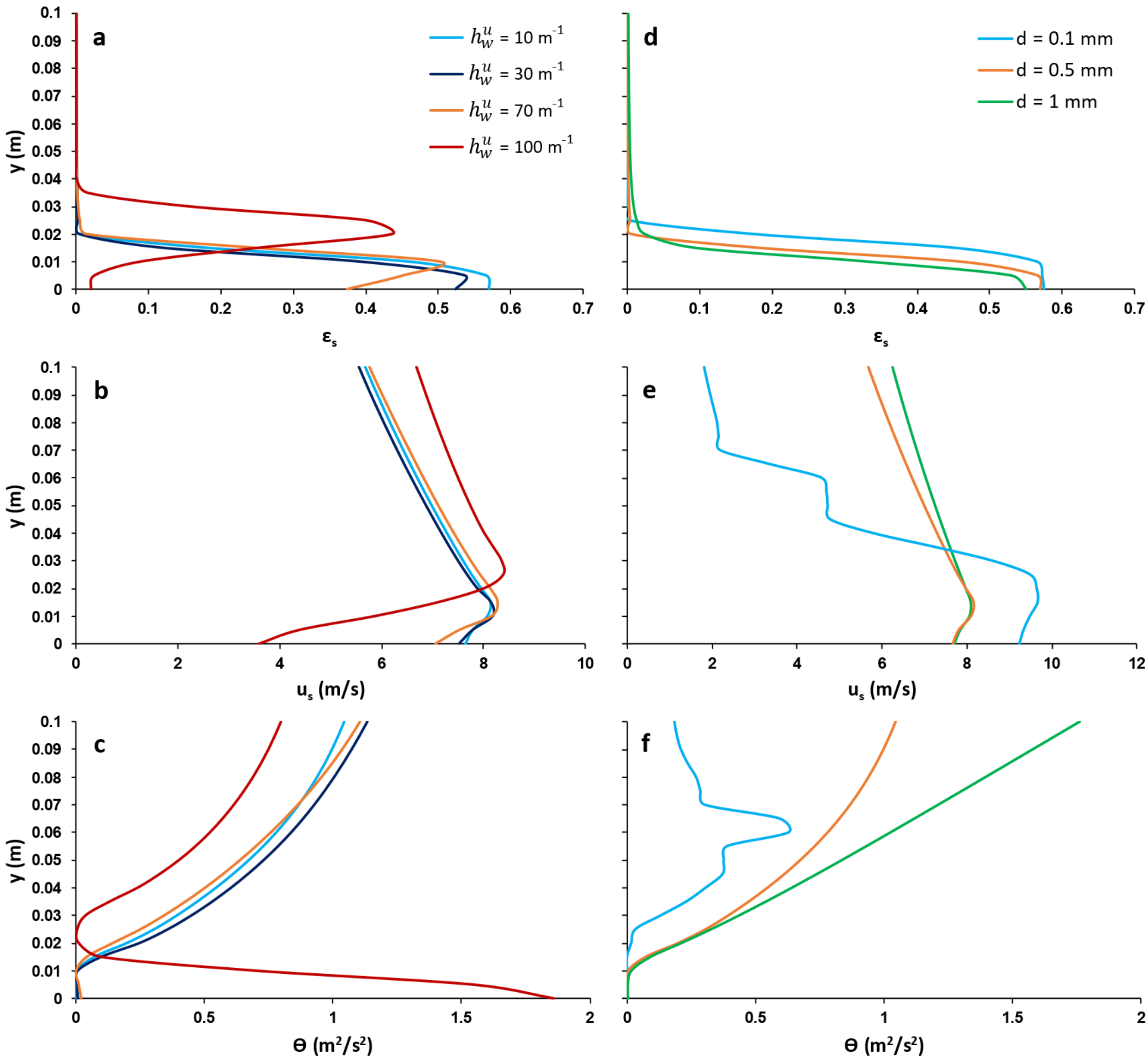

Figure 7. Profiles of solid volume concentration (a, d), solid velocity in x-direction (b, e) and granular temperature (c, f) at 9 m from the right side of the domain (or 5.5 m downstream the initial position of the granular material) against the distance from the wall at changing h_w^u and d. On the basis of the analytical profiles of θ and U (Section 2.3), c_w and h_w^{θ} were set to 0.1 kg s^{-3} and 10 kg m^{-2}s^{-1}, respectively.

The vertical profiles of ε_s, u_s and θ at increasing h_w^u show the air-cushion is generated for $h_w^u \geq 70$ m^{-1}, which leads to a flow thickness increase from 0.015 m to 0.030 m (Figs. 6 and 7a); the basal layer affected by the air-cushion results in lower u_s, which decreases from 7.65 m s^{-1} (h_w^u = 10 m^{-1}) to 3.59 m s^{-1} (h_w^u = 100 m^{-1}) (Fig. 7b); θ values are significantly influenced by varying h_w^u, with the highest value of 1.86 m^2 s^{-2} recorded at the boundary for the granular flow that generates the thickest air-cushion (h_w^u = 100 m^{-1}) (Fig. 7c). Instead, the simulations at increasing show flow thicknesses that decrease from 0.15 m to 0.05 m (Fig 7d) and maximum values decreasing from 9.65 m s^{-1} to 8.15 m s^{-1} (Fig. 7e). Furthermore, the vertical velocity profile for d = 0.1 mm is affected by a staircase-like trend with reducing values to the channel surface (Fig. 7e). Profiles for d = 0.5, 1 mm show a gradual decrease to the base of the flow with values close to 0 m^2 s^{-2}, while profile for d = 0.1 mm is more complex and exhibits almost neutral values near the channel surface that gradually increase in the flow centre reaching a granular temperatures peak at around 65 % of the flow height and then decrease to the flow top (Fig. 7f). The velocity staircase-like profile and the granular temperature peak are probably associated to the vortex activity, which interacts with the velocity of the finest solid phase (d = 0.1 mm).

These simulations were repeated by changing h_w^θ and c_w and by dropping the mono-disperse granular material both on the sloped (40°) and horizontal channel. Results can be found in the Supplementary Material (Appendix).

3. **Comparison between the different boundary conditions**

The results of ε_s for the different boundary conditions (Section 2.2.2, 2.2.3 and 2.2.4) showed the generation of an air-cushion layer at the base of the simulated granular flows either using the Johnson and Jackson boundary condition with $\phi \geq 0.1$ (Fig. 4) or manually setting h_w^u to values higher than 70 m^{-1} (Fig. 8). ε_s profiles recorded by granular flows with d = 0.5 mm for the different boundary conditions are compared in the Figure 8.

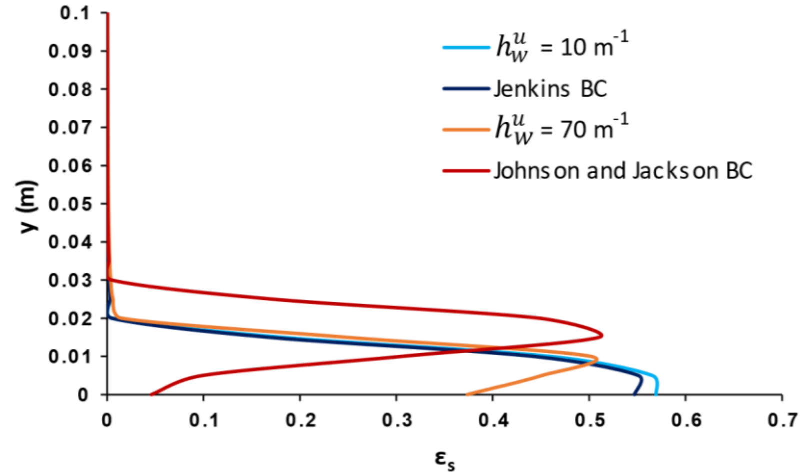

Figure 8. Profile of solid volume concentration for different boundary conditions at 9 m from the right side of the domain (or 5.5 m downstream the initial position of the granular material) against the distance from the wall. BC = boundary condition.

The comparison suggests the air-cushion dependence on high values of h_w^u. In order to verify this observation, in the simulations with mono-disperse granular material (d = 0.5 mm) we tracked the value of h_w^u at a fixed location (the boundary cell at 9 m of the sloped channel) over the duration at changing boundary conditions (Fig. 9). In addition to Johnson and Jackson and Jenkins boundary conditions, the Johnson and Jackson BC revisited by Li and Benyahia (2012) was also tested, which allows a predictive local calculation of ϕ (Eq. 16). The effects of the predictive ϕ on h_w^u calculation and consequently, on the air-cushion propagation at the flow base are well captured by the comparing plots of the gas volume concentration between the different boundary conditions (Fig. 10).

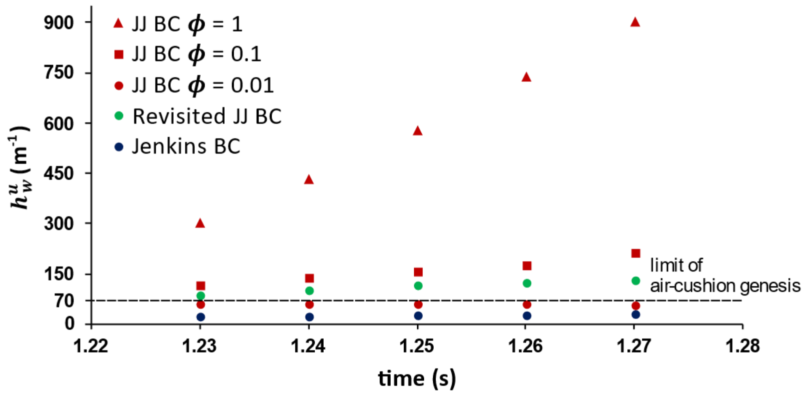

Figure 9. h_w^u iteratively calculated as a function of time. The plotted values refer to a position of 9 m of the sloped channel. The dotted line indicates the limit of air-cushion formation located to h_w^u = 70 m^{-1}. BC = boundary condition. JJ = Johnson and Jackson.

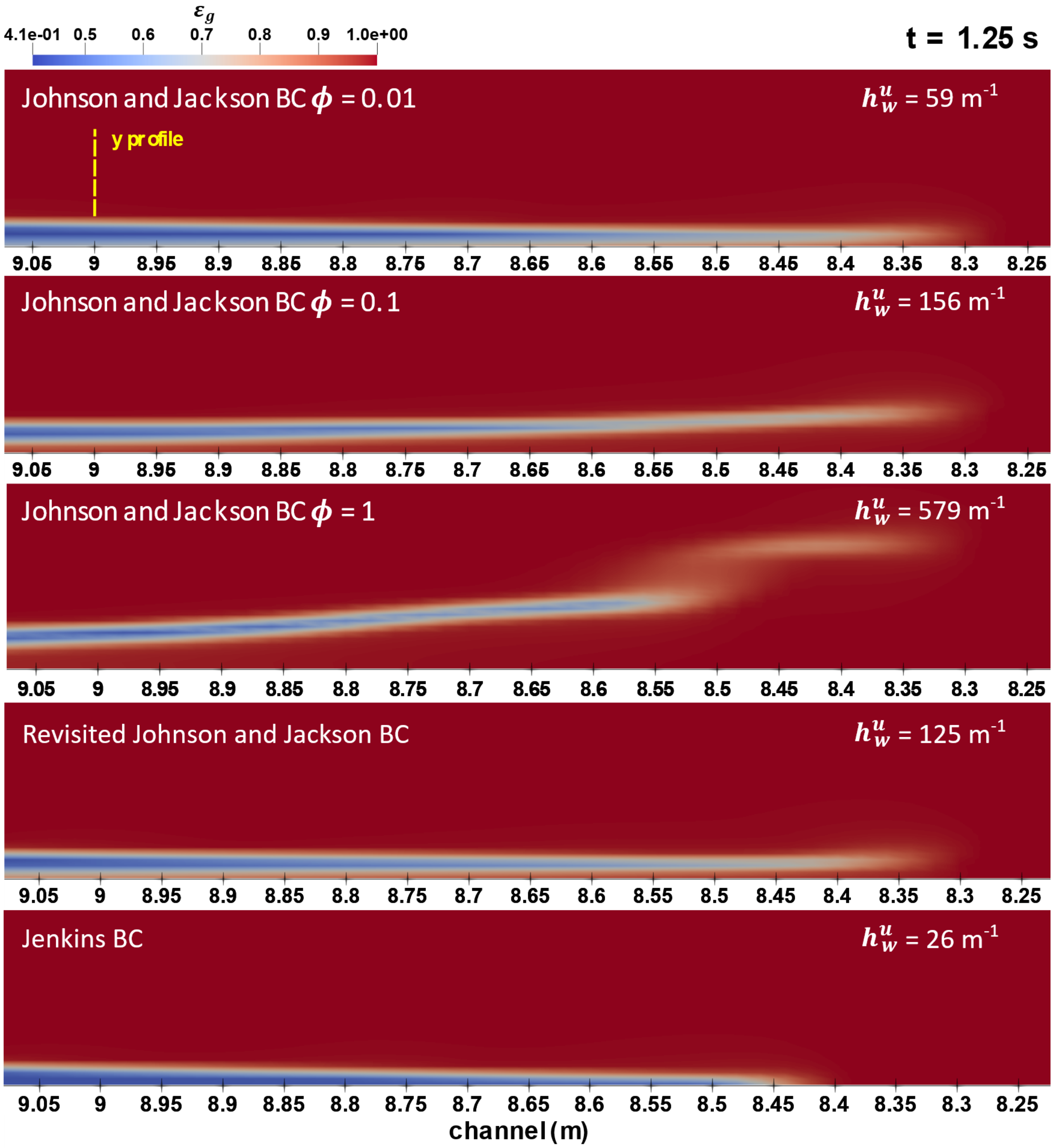

Figure 10. Plot of gas volume concentration (ε_g) of revisited and standard (by varying ϕ) Johnson and Jackson and Jenkins boundary conditions (BC). The yellow dotted line marks the profiles position shown in Figure 5, 7, 8 and 9. t = simulation time.

The Johnson and Jackson BC with $\phi \geq 0.1$ and the revisited Johnson and Jackson BC computed values of h_w^u that increase over time during the granular flow front passage from the control position. The values of h_w^u are significantly higher than the previously identified limit of the air-cushion formation at h_w^u = 70 m^{-1} (Fig. 9). On the other hand, the Johnsons and Jackson BC with ϕ = 0.01 and the Jenkins BC generate values of h_w^u lower than 70 m^{-1}, which resulted in simulated mono-disperse granular flows without the air-cushion at the flow base (Fig. 10). This proves the positive correlation between the air-cushion and the wall velocity transfer coefficient h_w^u. Furthermore, the iteratively calculated ϕ by Li and Benyahia equation (Eq. 16) slightly affect the simulations, resulting in lower h_w^u and in a less developed air-cushion (Fig. 10).

4. Comparing MFIX simulations with one large-scale experiment

The Johnson and Jackson (1987) and the Jenkins (1992) boundary conditions for the solid phase were used to model one of the granular flows produced at the large-scale flume facility at the University of San Luis Potosì (UASLP, Mexico) (Sulpizio et al., 2016). This represents a preliminary test of the ability of a specific boundary condition to quantify the velocities of the granular flow at the wall.

The instrumental apparatus used for the large-scale experiment comprises a hopper with a remotely controlled gate located 0.40 m above the hopper inlet of a 5-m long and 0.30-m wide flume with a 40° slope. More details on the apparatus and granular flows experiments are available in the works of Rodriguez-Sedano et al. (2016) and of Sulpizio et al. (2016). In the analysed experiment, 41.4 kg of solid particles of volcanic origin with a density $\rho_s \cong 2300$ kg/m^3 sieved within the diameter interval of 1 mm - 2 mm were used. Internal friction angle of the solid mixture (δ_{int}) was experimentally measured to be 33°. Granular flow front velocities were detected by seven laser barriers deployed along the whole channel flume length starting from 1.65 m downstream and evenly spaced of 0.45 m.

The numerical simulations were conducted by reproducing the particle release from the hopper via the collapse of a volume composed of mono-disperse mixture with d = 1 mm from a height of 0.40 m on a 40° inclined channel, which in turn was reproduced by tilting the acceleration components as seen in Section 2.2.1 (Fig. 3). The lower limit of the experimental diameter interval was selected to obtain the finest grid (0.01 m x 0.01 m) maintaining the TFM assumption on the size of the control volume that has to be at least ten times greater to the particles one. The rectangular computational domain of 7.5 m x 1.8 m was discretised via variable-sized rectangular cells with decreasing size down to square cells of 0.01 m side in the compacting and sliding zone (Fig. 11).

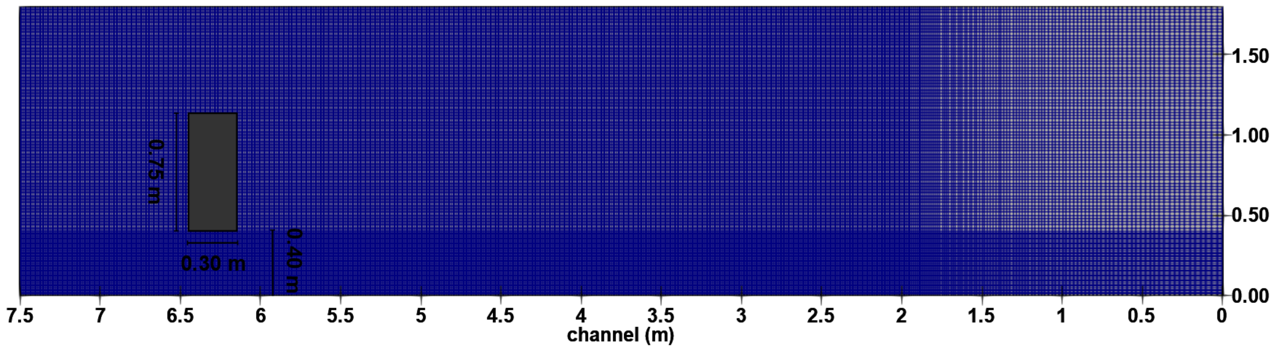

Figure 11. Grid layout for the computational domain. The granular material is shaded grey.

We performed the simulations by setting the partial-slip wall boundary condition for the solid phase and varying the partial-slip wall boundary conditions (Jenkins (1992) and Johnson and Jackson (1987)) and, when using the Johnsons and Jackson BC, by varying ϕ.

We compared experimental and simulated granular flow front velocities and those are reported in Fig. 12.

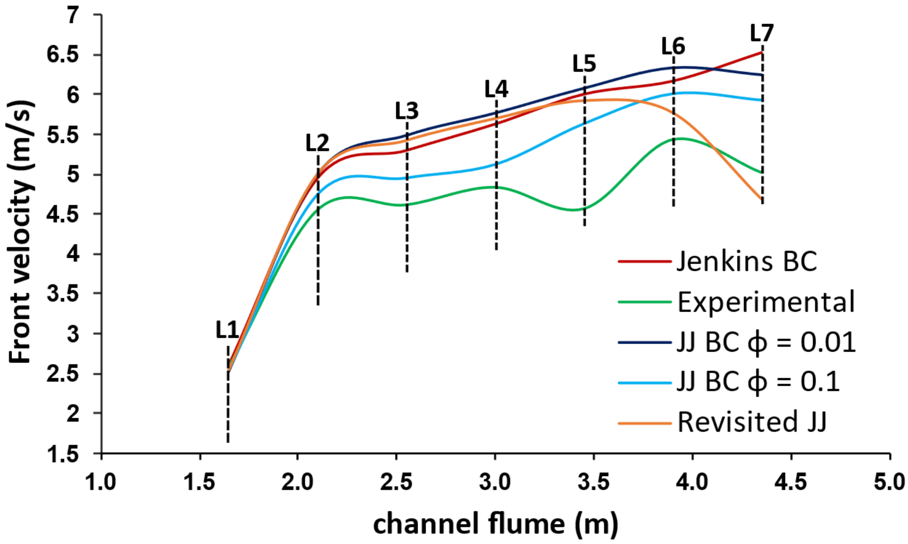

Figure 12. Simulated and experimental granular flow front velocities plotted along the channel flume. The black dotted lines indicate the laser detectors (L) position along the channel. JJ = Johnson and Jackson. BC = boundary condition.

In the experiment, the kinetic energy of the granular material released from the hopper is redirected along the channel flume upon impact on the channel, resulting in flow elongation and fast velocity increase in the first two meters of runout. The rapid velocity increase is followed by an oscillatory trend of front propagation velocities around ca. 4.0 m s^{-1} with a final larger velocity peak of 5.4 m s^{-1}. The simulated profiles show different behaviours upon changing the boundary conditions (Fig. 12). Jenkins BC and Johnson and Jackson BC with ϕ = 0.1 (air-cushion-forming), well mimic the experimental oscillatory trend from L2 to L4, with a better match for Johnson and Jackson BC, which develops a mean square error of 0.36 m^2 s^{-2} against an error of 0.88 m^2 s^{-2} obtained for Jenkins BC. Further downstream, the simulated velocities obtained with Jenkins BC and Johnson and Jackson BC increase reaching maximum values of 6.5 m s^{-1} and 6.0 m s^{-1}, respectively (Fig. 12). On the other hand, the Johnson and Jackson BC with ϕ = 0.01 (not air-cushion-forming) does not capture the experimental velocity oscillations showing a linear velocity increase, with a maximum velocity of 6.25 m s^{1} reached at L6 (Fig. 12) and with a mean square error of 0.93 m^2 s^{-2}. Finally, the revisited Johnson and Jackson BC follows the trend of the previous one up to L5 and then decreases approaching a velocity of 4.7 m s^{-1} (Fig. 12), resulting in a mean square error of 0.53 m^2 s^{-2}. Therefore, the boundary conditions air-cushion-forming seem to provide better results than BC not air-cushion forming nonetheless this phenomenon was not detected in the experimental granular flow.

5. Discussion and conclusions

Sensitivity analysis of the model to the different partial-slip boundary conditions for the solid phase available in the current version of MFIX were performed. The analysis showed that an air-cushion, at the contact between the solid phase and the wall, is generated when using the Johnson and Jackson (1987) boundary condition, while it never occurs when using Jenkins BC. The size (thickness) of the air-cushion was found to depend on the solid phase size and on to the specularity coefficient, a fact that is associated to the increase of the tangential momentum transferred to the wall by the solid phase collision as these parameters increase (second term of Eq. 14 and Eq. 15), which minimises the amount of slip at the wall, promoting diffuse collisions (greater ϕ) and eventually solid phase overpassing to the top flow. This in turn causes a decrease of the solid volume concentration, allowing the air-cushion formation and its maintenance during the flow slip. The flow sensitivity on the chosen value of ϕ was also demonstrated by other authors (Benyahia et al., 2005; Li et al., 2010b, 2010a). Additional simulations, with user-defined values of wall velocity transfer coefficient h_w^u for the solid phase, showed that this parameter plays a crucial role in the generation of the air-cushion, which occurs when $h_w^u > 70$ m^{-1} are used; the thickness of the air-cushion increases at increasing h_w^u. We further verified this by tracking h_w^u calculated by MFIX at specific location and time when using Johnson and Jackson and Jenkins boundary conditions and by comparing these values with the limit of the air-cushion formation (h_w^u = 70 m^{-1}; Fig. 9). In fact, simulations with Johnson and Jackson BC for ϕ of 1, 0.1 and 0.01 resulted in h_w^u of 579 m^{-1}, 156 m^{-1} and 59 m^{-1}, respectively, while simulations with Jenkins BC developed h_w^u of 26 m^{-1} (Fig. 10), hence confirming that the air-cushion is not formed or is roughly generated for boundary conditions predicting low values of h_w^u. The significantly different behaviour of these two boundary conditions is hence attributed to h_w^u calculation, which in the Johnson and Jackson BC strongly depends on the specularity coefficient ϕ (Table 2), which in turn represents an input data affected by great uncertainties since it is difficult to measure or estimate and usually is specified adjusting this parameter to fit some experimental data. The Johnson and Jackson boundary condition revisited by Li and Benyahia (2012), which calculates local values of the specularity coefficient (Eq. 16), was also tested resulting in h_w^u lower than those ones obtained by the standard Johnson and Jackson BC, but still greater than h_w^u of 70 m^{-1} (Figs. 9 and 10). Therefore, the revisited Johnson and Jackson BC does not avoid the air-cushion generation, but nonetheless reduce it controlling h_w^u calculation by means of a modelled ϕ. This again confirms the correlation between the air-cushion formation and the wall velocity transfer coefficient h_w^u. The possibility to manually set h_w^u, h_w^θ and c_w proved to be a powerful instrument to better understand the implication of h_w^u calculation on the air-cushion formation. However, the use of constant coefficients limits the model predictivity, considering that the manually set h_w^u, h_w^θ and c_w are time-independent and applied to all the partial-slip wall boundary conditions of the whole computational domain.

All granular flows reproduced by Sulpizio et al. (2016) and by Rodriguez-Sedano et al. (2016), including the here presented one, did not detect the air-cushion phenomenon, showing instead a basal layer that slip in frictional contact with the basal surface. However, it should be noted that the air-cushion could be difficult to experimentally capture, because the laboratory instruments (e.g. laser detectors, high-speed cameras, load cells etc.) are not adequate or not able to detect a phenomenon acting in a very limited basal region. Recently, Lube et al. (2019) showed by coupling large-scale experiments on dilute pyroclastic density currents and numerical multiphase modelling (MFIX-DEM) the generation of air lubrication at the base of the flow. Despite the dilute pyroclastic density currents and granular flows being very different, the work by Lube and co-workers lead to think to the air-cushion as a real phenomenon not detected during the granular flows experiments of Sulpizio et al. (2016) and of Rodriguez-Sedano et al. (2016). Many experiments on granular flows with different granulometries are still required to better evaluate the nature and the magnitude of the air-cushion phenomenon.

We finally carried out a benchmark of the boundary conditions implemented in MFIX against the experimental ones observed in a large-scale flume (Rodriguez-Sedano et al., 2016; Sulpizio et al., 2016). It should be noted that this benchmark study represents a preliminary analysis, since several experiments should be considered for a full investigation. The experimental flow front velocities exhibited a flow acceleration in the first two metres of the sloped channel followed by an oscillatory trend (Fig. 12). The initial flow acceleration is given by the redirection of the falling material kinetic energy along the channel flume, causing the flow elongation. The latter increases the frictional forces at the base promoting the overpassing of the coarser particles with great inertia into the upper layer and into the granular flow front. The high inertia held by the coarser particles and their upward and forward movement result in thicker and faster granular flow, which in turn promotes the flow elongation and the frictional forces at the flow base. Thinning and thickening alternance given by frictional and inertial forces competition explains the oscillatory velocity trend of the experimental granular flow front (Fig. 12). This velocity fluctuation was detected by MFIX simulations when using the Jenkins and the Johnson and Jackson models. In particular, simulations with Johnson and Jackson setting ϕ = 0.1 (air-cushion forming) resulted in the best match with the experimental data (Fig. 12) (mean square error of 0.36 m^2 s^{-2}), unlike the simulation with ϕ = 0.01 (not air-cushion-forming), which resulted in the worst match (Fig. 12) (mean square error of 0.93 m^2 s^{-2}). The revisited Johnson and Jackson BC (mean square error of 0.93 m^2 s^{-2}) developed a velocity decrease in proximity of the last two laser detectors, which is likely due to the fact that this boundary condition includes an expression for the specularity coefficient, which therefore responds to local changes of the flow parameters, influencing the simulated flow velocity. Generally, all the simulations resulted in velocities greater than observed ones. It should be note that: 1) since we are running a 2D simulation of a 3D phenomenon, we are neglecting the friction effects due to the sidewalls and adjacent particles; 2) the wall friction angle of 11° is probably not realistic for the case under analysis that is characterized by a channel roughness. In conclusion, the boundary conditions forming the air-cushion developed the best results nonetheless this phenomenon was not detected in the real granular flow. This outcome is probably due to a more realistic transfer of tangential momentum to the wall ruled by the specularity coefficient, which promotes the air-cushion formation and strongly influences the flow velocity. This preliminary analysis would seem to suggest the use of the Johnson and Jackson BC to replicate dense granular flows, even though additional comparisons between simulated and experimental data are required to exhaustively define which of the studied boundary conditions is the more appropriate to study this type of flows.

Acknowledgment

RO kindly acknowledges the financial support from the EPSRC (grant no. EP/N034066/1). This work was in part funded by the British Geological Survey University Funding Initiative (BUFI) PhD studentship (S385). This work is published with permission of the Executive Director of British Geological Survey (UKRI).

Appendix

In addition to the analysis of the influence of h_w^u, simulations with different d were conducted setting h_w^u to 10 m^{-1} and simulating the fall of a mono-disperse granular material of 0.5 mm on a 40° sloped channel. Results are reported in Figure 13.

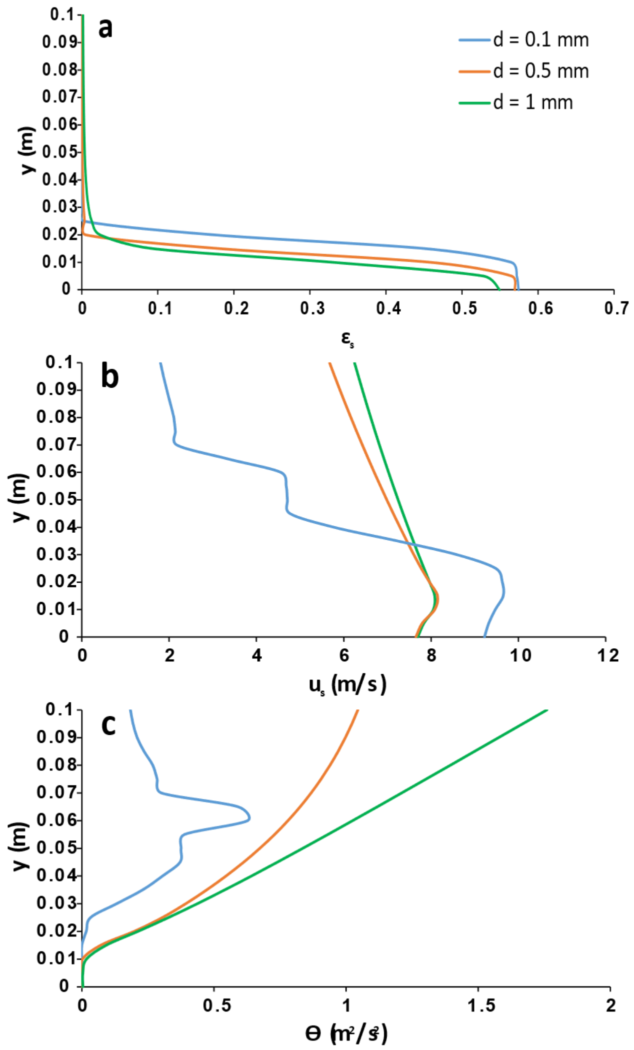

Figure 13. Profiles of solid volume concentration (a), solid velocity in x-direction (b) and granular temperature (c) at 9 m from the right side of the domain (or 5.5 m downstream the initial position of the granular material) against the distance from the wall at changing d. On the basis of the analytical profiles of θ and v (Section 2.3), c_w was set to 0.1 kg s^{-3} and h_w^{θ} was set to 10 kg m^{-2}s^{-1}. t = 1.25 s.

ε_s profiles for the different solid phase sizes have very similar shapes with thicker flows for the smaller particles (Fig. 13a). u_s profiles exhibit greater velocities for particles diameter of 0.1 mm, which is affected by a staircase-like trend with decreasing values to the channel surface (Fig. 13b). θ profiles for d equals to 0.5 mm and 1 mm show a gradual decrease to the basal layer with values close to 0, while the granular flow with d = 0.1 mm records a granular temperatures peak (Fig. 13c). The velocity staircase-like profile and the granular temperatures peak are probably associated to the vortex activity, which negatively interacts with the solid phase velocity.

Numerical simulations at changing h_w^θ and c_w were run simulating mono-disperse granular material of 0.5 mm falling both on sloped (40°) and horizontal channel. Profiles obtained for the sloped channel at changing coefficients were almost identical between them and very similar to the horizontal ones. For this reason, we only reported the simulations results for the horizontal channel for h_w^θ equal to 1 kg $m^{-2}s^{-1}$, 10 kg $m^{-2}s^{-1}$, 100 kg $m^{-2}s^{-1}$ and c_w equal to 0.1 kg s^{-3}, 1 kg s^{-3} and 10 kg s^{-3} (Fig. 14).

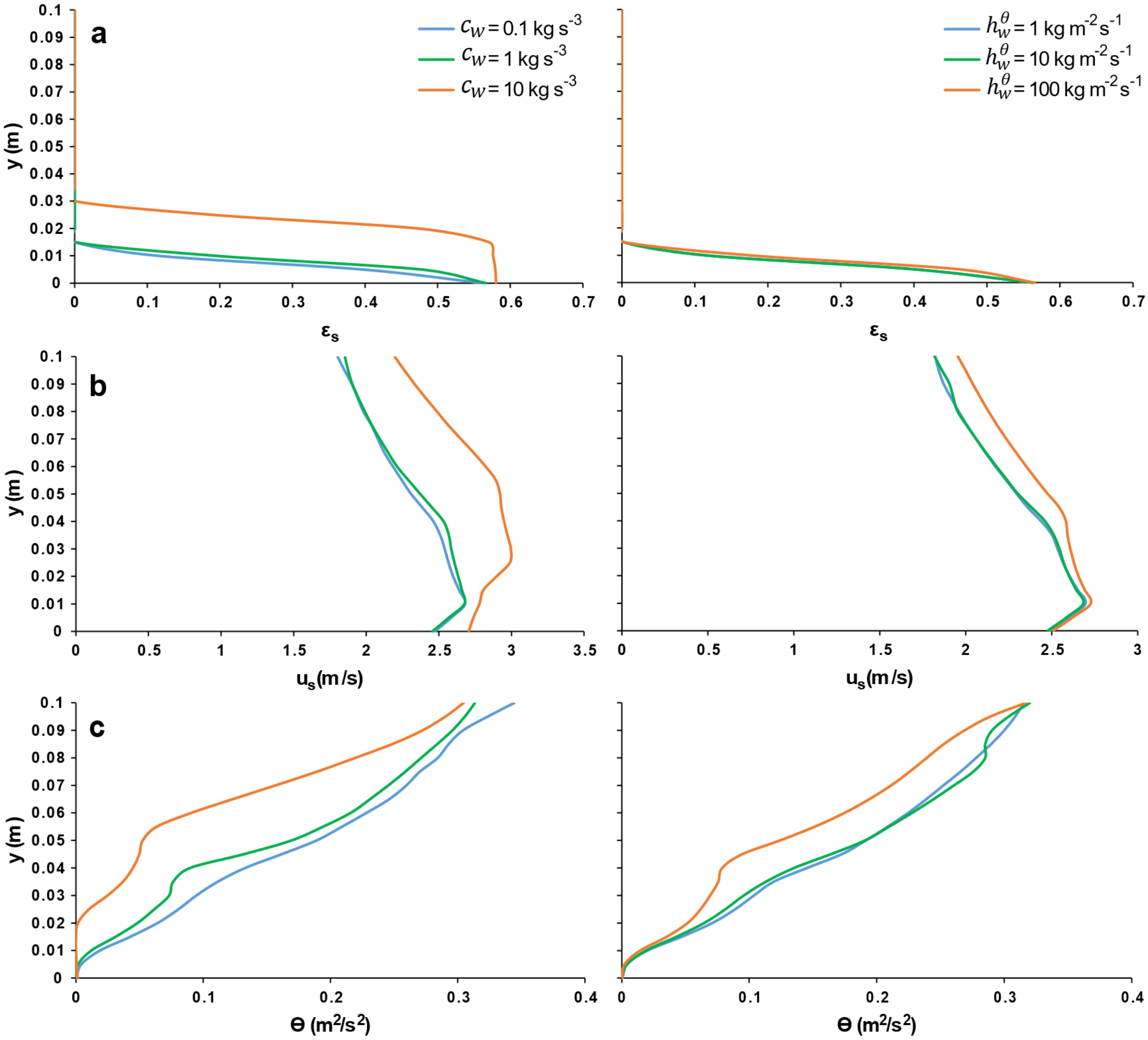

Figure 14. Profiles of solid volume concentration (a), solid velocity in x-direction (b) and granular temperature (c) at 9 m from the right side of the domain (or 5.5 m downstream the initial position of the granular material) against the distance from the wall at changing h_w^θ and c_w. On the basis of the analytical profiles of θ and v (Section 2.3), c_w was set to 0.1 kg s^{-3} for simulations changing h_w^θ, and h_w^θ was set to 10 kg m^{-2}s^{-1} for simulations changing c_w. h_w^u was set to 10 m^{-1} for the same reason. t = 1.25 s.

The solid volume concentration profiles show almost imperceptible variations for simulations with different h_w^θ and slight difference for simulations changing c_w. In particular, c_w = 10 kg s^{-3} results in a simulated flow 0.014 m thicker than simulations with lower c_w (Fig. 14a). u_s profiles for all values of h_w^θ and c_w exhibit very similar trends, with the profile for c_w = 0.1 kg s^{-3} and h_w^θ = 100 kg m^{-2}s^{-1}

that show the greatest velocities (Fig. 14b). Finally, θ shows trends that linearly decrease to the basal part until values close to 0 m^2 s^{-2} (Fig. 14c).

References

Anderson, T.B., Jackson, R., 1967. Fluid Mechanical Description of Fluidized Beds. Ind. Eng. Chem. Fundam. 6, 527–539. https://doi.org/10.1021/i160024a007

Benyahia, S., Syamlal, M., O'Brien, T.J., 2005. Evaluation of boundary conditions used to model dilute, turbulent gas/solids flows in a pipe. Powder Technol. 156, 62–72. https://doi.org/10.1016/j.powtec.2005.04.002

Boyle, E.J., Massoudi, M., 1989. A kinetic theory derivation of the stress tensor for granular material that includes normal stress effects, Tech. Rep. DOE/METC-89/4088, DE89 00,977, 66 pp., U.S. Dep. of Energy, Washington, D. C.

Branney, J.M., Kokelaar, P., 2002. Pyroclastic density currents and the sedimentation of ignimbrites, Geological Society Memoir No. 27. https://doi.org/10.1086/427850

Breard, E.C.P., Dufek, J., Roche, O., 2019. Continuum Modeling of Pressure-Balanced and Fluidized Granular Flows in 2-D: Comparison With Glass Bead Experiments and Implications for Concentrated Pyroclastic Density Currents. J. Geophys. Res. Solid Earth 1–27. https://doi.org/10.1029/2018JB016874

Campbell, C.S., 1990. Rapid Granular Flows. Annu. Rev. Fluid Mech. 22, 57–90. https://doi.org/10.1146/annurev.fl.22.010190.000421

Cundall, P.A., Strack, O.D.L., 1979. A discrete numerical model for granular assemblies. Geotechnique 29, 47–65. https://doi.org/10.1680/geot.1979.29.1.47

Dartevelle, S., 2004. Numerical modeling of geophysical granular flows: 1. A comprehensive approach to granular rheologies and geophysical multiphase flows. Geochemistry, Geophys. Geosystems 5. https://doi.org/10.1029/2003GC000636

Garg, R., Galvin, J., Li, T., Pannala, S., 2012. Open-source MFIX-DEM software for gas-solids flows: Part I-Verification studies. Powder Technol. 220, 122–137. https://doi.org/10.1016/j.powtec.2011.09.019

Ge, W., Lu, L., Liu, S., Xu, J., Chen, F., Li, J., 2015. Multiscale Discrete Supercomputing – A Game Changer for Process Simulation? Chem. Eng. Technol. 38, 575–584.

Gera, D., Syamlal, M., O'Brien, T.J., 2004. Hydrodynamics of particle segregation in fluidized beds. Int. J. Multiph. Flow 30, 419–428. https://doi.org/10.1016/j.ijmultiphaseflow.2004.01.003

Hanes, D.M., Inman, D.L., 1985. Observations of rapidly flowing granular-fluid materials. J. Fluid Mech. 150, 357–380.

Harnett, C.E., Thomas, M.E., Purvance, M.D., Neuberg, J., 2018. Using a discrete element approach to model lava dome emplacement and collapse. J. Volcanol. Geotherm. Res. 359, 68–77.

Hui, K., Haff, P.K., Ungar, J.E., Jackson, R., 1984. Boundary conditions for high-shear grain flows. J. Fluid Mech. 145, 223–233. https://doi.org/10.1017/S0022112084002883

Iverson, R.M., 1997. The Physics of Debris Flows. Rev. Geophys. 35, 245–296. https://doi.org/10.1029/97RG00426;

Iverson, R.M., Vallance, J.W., 2001. New views of granular mass flows. Geology 29, 115–118. https://doi.org/10.1130/0091-7613(2001)029<0115:NVOGMF>2.0.CO;2

Jaeger, H.M., Nagel, S.R., Behringer, R.P., 1996. The physics of granular materials. Phys. Today 49, 32–38. https://doi.org/10.1063/1.881494

Jenike, A.W., 1987. A theory of flow of particulate solids in converging and diverging channels based on a conical yield function. Powder Technol. 50, 229–236. https://doi.org/10.1016/0032-5910(87)80068-2

Jenkins, J.T., 1992. Boundary conditions for rapid granular flow: Flat, frictional walls. J. Appl. Mech. Trans. ASME. https://doi.org/10.1115/1.2899416

Johnson, P.C., Jackson, R., 1987. Frictional-collisional constitutive relations for granular materials, with application to plane shearing. J. Fluid Mech. 176, 67–93. https://doi.org/10.1017/S0022112087000570

Jop, P., Forterre, Y., Pouliquen, O., 2005. Crucial role of sidewalls in granular surface flows: Consequences for the rheology. J. Fluid Mech. 541, 167–192. https://doi.org/10.1017/S0022112005005987

Li, T., Benyahia, S., 2012. Revisiting Johnson and Jackson boundary conditions for granular flows. AIChE J. 58, 2058–2068. https://doi.org/10.1002/aic.12728

Li, T., Garg, R., Galvin, J., Pannala, S., 2012. Open-source MFIX-DEM software for gas-solids flows: Part II - Validation studies. Powder Technol. 220, 138–150. https://doi.org/10.1016/j.powtec.2011.09.020

Li, T., Grace, J., Bi, X., 2010a. Study of wall boundary condition in numerical simulations of bubbling fluidized beds. Powder Technol. 203, 447–457.

Li, T., Zhang, Y., Grace, J.R., Bi, X., 2010b. Numerical investigation of gas mixing in gas-solid fluidized beds. AIChE J. 56, 2280–2296.

Louge, M.Y., Turnbull, B., Carroll, C., 2012. Volume growth of a powder snow avalanche. Ann. Glaciol. 53, 57–60. https://doi.org/10.3189/2012AoG61A030

Lube, G., Breard, E.C., Jones, J., Fullard, L., Dufek, J., Cronin, S.J., Wang, T., 2019. Generation of air lubrication within pyroclastic density currents. Nat. Geosci. 12, 381–386.

Lun, C.K.K., Savage, S.B., Jeffrey, D.J., Chepurniy, N., 1984. Kinetic theories for granular flow: Inelastic particles in Couette flow and slightly inelastic particles in a general flowfield. J. Fluid Mech. 140, 223–256. https://doi.org/10.1017/S0022112084000586

Neglia, F., Sulpizio, R., Dioguardi, F., Capra, L., Sarocchi, D., 2020. Shallow-water models for volcanic granular flows: A review of strengths and weaknesses of TITAN2D and FLO2D numerical codes. J. Volcanol. Geotherm. Res. 107146.

Pritchett, J.W., Blake, T.R., Garg, S.K., 1978. Numerical model of gas fluidized beds, in: AIChE Symp Ser.

Rodriguez-Sedano, L.A., Sarocchi, D., Sulpizio, R., Borselli, L., Campos, G., Moreno Chavez, G., 2016. Influence of particle density on flow behavior and deposit architecture of concentrated pyroclastic density currents over a break in slope: Insights from laboratory experiments. J. Volcanol. Geotherm. Res. https://doi.org/10.1016/j.jvolgeores.2016.10.017

Sarno, L., Carleo, L., Papa, M.N., Villani, P., 2018a. Experimental Investigation on the Effects of the Fixed Boundaries in Channelized Dry Granular Flows. Rock Mech. Rock Eng. 51, 203–225. https://doi.org/10.1007/s00603-017-1311-2

Sarno, L., Carravetta, A., Tai, Y.C., Martino, R., Papa, M.N., Kuo, C.Y., 2018b. Measuring the velocity fields of granular flows – Employment of a multi-pass two-dimensional particle image velocimetry (2D-PIV) approach. Adv. Powder Technol. 29, 3107–3123.

https://doi.org/10.1016/j.apt.2018.08.014

Savage, S.B., 1998. Analyses of slow high-concentration flows of granular materials. J. Fluid Mech. 377, 1–26. https://doi.org/10.1017/S0022112098002936

Savage, S.B., Sayed, M., 1984. Stresses developed by dry cohesionless granular materials sheared in an annular shear cell. J. Fluid Mech. 142, 391–430.

Schaeffer, D.G., 1987. Instability in the evolution equations describing incompressible granular flow. J. Differ. Equ. https://doi.org/10.1016/0022-0396(87)90038-6

Srivastava, A., Sundaresan, S., 2003. Analysis of a frictional-kinetic model for gas-particle flow. Powder Technol. 129, 72–85. https://doi.org/10.1016/S0032-5910(02)00132-8

Sulpizio, R., Capra, L., Sarocchi, D., Saucedo, R., Gavilanes-Ruiz, J.C., Varley, N.R., 2010. Predicting the block-and-ash flow inundation areas at Volcán de Colima (Colima, Mexico) based on the present day (February 2010) status. J. Volcanol. Geotherm. Res. 193, 49–66. https://doi.org/10.1016/j.jvolgeores.2010.03.007

Sulpizio, R., Castioni, D., Rodriguez-Sedano, L.A., Sarocchi, D., Lucchi, F., 2016. The influence of slope-angle ratio on the dynamics of granular flows: insights from laboratory experiments. Bull. Volcanol. 78, 77. https://doi.org/10.1007/s00445-016-1069-5

Syamlal, M., Rogers, W., O`Brien, T.J., 1993. MFIX documentation theory guide. DOE/METC-94/1004, DE9400,097. USDOE Morgant. Energy Technol. Center, WV. https://doi.org/10.2172/10145548

Valentine, G.A., 2020. Initiation of dilute and concentrated pyroclastic currents from collapsing mixtures and origin of their proximal deposits. Bull. Volcanol. 82. https://doi.org/10.1007/s00445-020-1366-x

Valentine, G.A., Sweeney, M.R., 2018. Compressible Flow Phenomena at Inception of Lateral Density Currents Fed by Collapsing Gas-Particle Mixtures. J. Geophys. Res. Solid Earth 123, 1286–1302. https://doi.org/10.1002/2017JB015129

Zanchetta, G., Sulpizio, R., Pareschi, M.T., Leoni, F.M., Santacroce, R., 2004. Characteristics of May 5-6, 1998 volcaniclastic debris flows in the Sarno area (Campania, southern Italy): Relationships to structural damage and hazard zonation. J. Volcanol. Geotherm. Res. 133, 377–393. https://doi.org/10.1016/S0377-0273(03)00409-8